Highly ethylene-selective electrocatalytic CO2 reduction enabled by isolated Cu-S motifs in metal-organic framework-based precatalysts

Wen, C. F., Zhou, M., Liu, P. F., Liu, Y., Wu, X., Mao, F., Dai, S., Xu, B., Wang, X. L., Jiang, Z., Hu, P., Yang, S., Wang, H. F., & Yang, H. (2022). Highly ethylene-selective electrocatalytic CO2 reduction enabled by isolated Cu-S motifs in metal-organic framework-based precatalysts. *Angewandte Chemie International Edition*, *61*(2), Article e202111700. https://doi.org/10.1002/anie.202111700

Published in:
Angewandte Chemie International Edition

Document Version:
Peer reviewed version

A Journal of the Gesellschaft Deutscher Chemiker

Angewandte International Edition GDCh Chemie

www.angewandte.org

Accepted Article

Title: Highly ethylene-selective electrocatalytic CO2 reduction enabled by isolated Cu-S motifs in metal-organic framework-based precatalysts

Authors: Chun Fang Wen, Min Zhou, Peng Fei Liu, Yuanwei Liu, Xuefeng Wu, Fangxin Mao, Sheng Dai, Beibei Xu, Xue Lu Wang, Zheng Jiang, Peijun Hu, Shuang Yang, Hai Feng Wang, and Huagui Yang

To be cited as: *Angew. Chem. Int. Ed.* 10.1002/anie.202111700

Link to VoR: https://doi.org/10.1002/anie.202111700

WILEY-VCH

10.1002/anie.202111700

RESEARCH ARTICLE

WILEY-VCH

Highly ethylene-selective electrocatalytic CO_2 reduction enabled by isolated Cu-S motifs in metal-organic framework-based precatalysts

Chun Fang Wen,[+[a]] Min Zhou,[+[b]] Peng Fei Liu,*[a] Yuanwei Liu,[a] Xuefeng Wu,[a] Fangxin Mao,[a] Sheng Dai,[c] Beibei Xu,[d] Xue Lu Wang,[d] Zheng Jiang,[e] P. Hu,[b,f] Shuang Yang,[a] Hai Feng Wang,*[b] and Hua Gui Yang*[a]

[a] C. F. Wen, Dr. P. F. Liu, Y. Liu, X. Wu, Dr. F. Mao, Prof. S. Yang and Prof. H. G. Yang
Key Laboratory for Ultrafine Materials of Ministry of Education, School of Materials Science and Engineering
East China University of Science and Technology
130 Meilong Road, Shanghai 200237, China
E-mail: hgyang@ecust.edu.cn, pfliu@ecust.edu.cn

[b] M. Zhou, Prof. P. Hu and Prof. H. F. Wang
Key Laboratory for Advanced Materials, School of Chemistry and Molecular Engineering
East China University of Science and Technology
130 Meilong Road, Shanghai 200237, China
E-mail: hfwang@ecust.edu.cn

[c] Prof. S. Dai
Key Laboratory for Advanced Materials and Feringa Nobel Prize Scientist Joint Research Center, Institute of Fine Chemicals, School of Chemistry and Molecular Engineering,
East China University of Science and Technology
130 Meilong Road, Shanghai 200237, China

[d] B. Xu and Prof. X. L. Wang
Physics Department and Shanghai Key Laboratory of Magnetic Resonance, School of Physics and Materials Science
East China Normal University
3663 North Zhongshan Road, Shanghai 200062, China

[e] Prof. Z. Jiang
Shanghai Synchrotron Radiation Facility
Shanghai Institute of Applied Physics, Chinese Academy of Sciences
Shanghai 201204, China

[f] Prof. P. Hu
School of Chemistry and Chemical Engineering
The Queen's University of Belfast
Belfast BT9 5AG, UK

[+] These authors contributed equally to this work.

Supporting information for this article is given via a link at the end of the document.

Abstract: Copper-based material is an efficient electrocatalyst for CO_2 conversion to C_{2+} products, most of which will reconstruct to *in-situ* regenerate active species. It is a challenge to precisely design precatalyst to obtain active sites for CO_2 reduction reaction (CO_2RR). Herein, we develop a local sulfur doping strategy over the Cu-based metal-organic frameworks precatalyst that disperses stable Cu-S motif in the framework of HKUST-1 (S-HKUST-1). The precatalyst exhibits a high ethylene selectivity in H-type cell with maximum faradaic efficiency (FE) of 60.0%, and delivers a current density of 400 mA cm^{-2} with ethylene FE to 57.2% in a flow cell. Operando X-ray absorption results demonstrate that $Cu^{\delta+}$ species stabilized by Cu-S motif exist in S-HKUST-1 during CO_2RR. Density functional theory calculations indicate the partially oxidized $Cu^{\delta+}$ at Cu/Cu_xS_y interface is favorable for *CO intermediate coupling due to the modest distance of coupling sites and optimized adsorption energy.

Introduction

The electrochemical reduction of carbon dioxide (CO_2) into value-added feedstocks is a desirable route to mitigate the depletion of fossil fuels and alleviate the greenhouse gas emissions[1]. The high-value multi-carbon (C_{2+}) hydrocarbons products *via* CO_2 reduction reaction (CO_2RR) are highly attractive due to their practical applications[2]; however, their selectivity and activity are severely limited by multi-step hydrogenation steps and competitive reactions[3]. Copper-based material is the most efficient electrocatalyst for selectively convert CO_2 to C_{2+} products[4], and its performance can be further influenced *via* modulating oxidation states[5], grain boundaries[6] and unsaturated sites[7]. It's worth noting that these structural features of copper-based material can be *in-situ* changed due to the precatalyst reconstruction under CO_2RR conditions. Taken copper oxides as a classic example, they usually act as CO_2RR precatalysts, which can be partially reduced to regenerate biphasic copper/copper oxide, coupled with abundant grain boundaries and unsaturated sites as active CO_2RR species, exhibiting significantly increased CO_2RR performance than the pure copper[5, 8].

Besides the widely reported copper oxides-based precatalysts[9], other copper-based compounds[10] have also been chosen as efficient precatalysts to introduce stable oxidized $Cu^{\delta+}$ species for C_{2+} production, due to the more stable Cu(X) (X means the B, N or other heteroatoms) species than the Cu(O) matrix under CO_2RR condition[10]. Unfortunately, these copper-based compounds could not elaborately regenerate abundant biphasic $Cu^{\delta+}$ species which features isolated Cu(X) species in the

reconstructed catalyst. It still remains as a big challenge to precisely control the local structure of precatalysts to regenerate stable and active sites under CO_2RR condition, especially for C_{2+} products. Unlike metal compounds, metal-organic frameworks-based (MOFs-based) material is an ideal precatalyst due to its controllable size/shape, high surface area, chemical tunability and the open metal sites[11], which affords a platform for incorporating isolated active species at atomic level. Therefore, we anticipate isolating stable Cu(X) species into the Cu-based MOFs precatalyst might regenerate homogeneously dispersed active sites under CO_2RR condition.

Herein, we rationally constructed isolated Cu-S motif on HKUST-1 precatalyst by a local sulfur doping strategy (S-HKUST-1). Although Cu(S)-based materials can electrochemically reduce CO_2 to major products of formate[12], some Cu(S) catalysts have recently been reported with enhanced CO_2 reduction selectivity to C_{2+} products[7], because of the local modification of geometric and electronic structure of Cu sites, which would influence its activity and selectivity. In this work, the S-HKUST-1 can be *in-situ* reconstructed to give Cu(S) matrix with abundant and active biphasic copper/copper sulfide (Cu/Cu_xS_y) interfaces, which can obtain a high ethylene (C_2H_4) selectivity in the H-type cell with the maximum faradaic efficiency (FE) of 60.0%, and delivers a current density of 400 mA cm^{-2} with FE_{C2H4} reaching up to 57.2% and FE_{C2} (FE of C_2H_4, C_2H_5OH and CH_3COOH) of 88.4% in the flow cell configuration. The systematic characterizations demonstrate the stable existence of Cu-S motif before and after CO_2RR. Density functional theory (DFT) calculations further reveal that the stabilized $Cu^{\delta+}$ at the Cu/Cu_xS_y interfaces featuring the modest distance of coupling sites and the optimized kinetic barrier for $^*CO$ intermediate dimerization. This work provides a new pathway to design efficient CO_2RR electrocatalyst *via* rationally constructing precatalysts at atomic scale.

Results and Discussion

Synthesis and local structural characterization of S-HKUST-1 precatalyst

The S-HKUST-1 precatalyst was prepared by a wet chemistry method, that is, a certain amount of as-prepared HKUST-1 was immersed in the ethanol solution of thioacetamide for 1 hour (h) at room temperature. It is mentionable that the thioacetamide slowly react with the contained water in the HKUST-1 to generate H_2S for construction of local Cu-S coordination[13], to give S-HKUST-1 precatalysts (Figures 1a and S1, see the Methods in Supplementary Information for details). The Cu-S motif could be atomically dispersed in the precatalyst and no aggregated copper sulfide could be generated if the amount of thioacetamide was elaborately controlled.

Both S-HKUST-1 and HKUST-1 precatalysts display the octahedral morphology (Figure S2), which were confirmed by scanning electron microscopy (SEM) characterizations. As shown in Figure S3, the scanning transmission electron microscopy (STEM)-based energy-dispersive X-ray spectroscopy (EDS) reveals that sulfur is distributed evenly throughout the S-HKUST-1 particle. Furthermore, sulfur can be observed on ultrathin slices of S-HKUST-1, which directly shows that sulfur is distributed within the whole S-HKUST-1 particle, instead of just on the surface of the catalyst (Figures S3b, S3d, S4, Tables S1 and S2). The X-ray diffraction (XRD) pattern of as-prepared HKUST-1 is similar to the simulated HKUST-1 reference, suggesting the successful synthesis of crystalline HKUST-1[14]. In addition, the XRD patterns of S-HKUST-1 (with different S contents) match well with HKUST-1 diffraction pattern, and no other crystalline species appeared (Figures 1b and S5), displaying that the framework structure of HKUST-1 was still maintained and no aggregated copper sulfide could be generated. From single-crystal X-ray diffraction (SXRD) data, the crystal data and structure refinement of S-HKUST-1 and HKUST-1 show no obvious change, which is similar to HKUST-1 reference (Figure S6, Tables S3 and S4).[15] As shown in Figure 1c, the Fourier transform infrared (FTIR) spectrum of S-HKUST-1 is nearly similar to that of HKUST-1, showing asymmetric vibration of O=C-O at 1645 cm^{-1}, 1450 cm^{-1}, symmetric vibration of O=C-O at 1374 cm^{-1}, vibration of C-O at 1114 cm^{-1}, and vibration of phenyl at 758 cm^{-1} and 731 cm^{-1}, respectively[16]. The Raman spectra also indicate that the framework structure and organic bonding of HKUST-1 are maintained after S incorporation (Figure S7). The amount of S element in S-HKUST-1 precatalyst was estimated based on the inductively coupled plasma optical emission spectrometry (ICP-OES) analysis and the elemental analysis (EA). The ICP-OES and EA data in the Tables S5 and S6 show that the weight fractions of S elements in S-HKUST-1 is 0.33 and 0.17 wt%, respectively.

The surface composition and elemental states of S-HKUST-1 and controlled sample were further characterized by X-ray photoelectron spectroscopy (XPS). Compared with that of HKUST-1, a broad S 2*p* peak is visible at 162.5 eV in S-HKUST-1, which is consistent with Cu-S bonding[12a, 17] (Figure 1d). This result unambiguously confirms the successful incorporation of S element in HKUST-1. In the XPS spectra of Cu $2p_{3/2}$ region, both S-HKUST-1 and HKUST-1 precatalysts possess a peak centered at the binding energy of 934.7 eV, which is attributed to Cu^{2+} species, demonstrating that partial Cu centers of the S-HKUST-1 still maintain coordination with trimesic acid. The peak at 932.4 eV associated with Cu^0/Cu^+ species was observed for S-HKUST-1 and HKUST-1[18]. The peak intensity for Cu^0/Cu^+ components significantly increases in S-HKUST-1 (Figure 1e), further suggesting that Cu^{2+} species were partially reduced after S incorporation to form Cu-S coordinated species. The Cu LMM auger spectra of HKUST-1 and S-HKUST-1 were measured for the further clarification of Cu valency (Figure S8). Compared with HKUST-1, S-HKUST-1 exhibits a broad peak at the binding energy of 570.0 and 567.9 eV, which indicates the presence of Cu^+ and Cu^0 [19]. Sulfur is lower electronegative than oxygen, so that the attract-electrons ability of S atoms is weak, which might lead to a relatively low valence of Cu. We speculate that the local Cu-O bond in HKUST-1 might be broken by the treatment of thioacetamide molecules for construction of Cu-S motif.

To confirm the transformation process from HKUST-1 to S-HKUST-1 proposed, the changes of oxidation states and local coordination environments of Cu atoms were investigated by X-ray absorption near-edge structure (XANES) and extended X-ray absorption fine structure (EXAFS) analyses, respectively. Figure S9 shows the high-quality *k*-space (k^3-weighted) Cu K-edge EXAFS spectra of HKUST-1, S-HKUST-1 and controlled Cu foil,

CuO, Cu_2S and Cu_2O samples, which can support the reliability of Fourier transformation (FT) of the EXAFS spectra[20]. The FT of EXAFS spectra for S-HKUST-1 and original HKUST-1 exhibit similar curves featuring a main peak at approximately 1.53 Å (without phase correction if not mentioned) arising from Cu-O bond (Figure 1f), suggesting that the main structure of HKUST-1 is maintained. When incorporating S elements into HKUST-1 to form S-HKUST-1, the Cu-O peak exhibits a remarkable intensity decrease, which is consistent with those reported in literatures[21], indicating that the water molecule directly linked with the Cu atoms are partially lost. Furthermore, the main Cu-O peak for S-HKUST-1 shifts to longer lengths, suggesting the expansion of the Cu-O bond due to the S incorporation to construct local Cu-S motif. From the XANES spectra of HKUST-1 and S-HKUST-1 (Figure 1g), two peaks were observed, including a pre-edge peak at 8981 eV corresponding to 1s→3d transition and a white-line peak at 8997 eV[21]. When S incorporated into the HKUST-1, the decreased intensity for the white line peak and the increased intensity for the 1s→3d peak indicate a change in the coordination of Cu centers, which is resulted from the removal of water molecule[22]. The obtained precatalysts with different S contents also exhibit the similar phenomena, indicating the increased intensity of Cu-O peak, the decreased intensity of white line peak and the increased intensity of the 1s→3d peak (Figure S10). The electron paramagnetic resonance (EPR) signal intensity of S-HKUST-1 also increases and the peak becomes sharper compared to the HKUST-1, indicating that the Cu microstructure has changed[16] (Figure 1h). As shown in Figure S11, the BET surface area of S-HKUST-1 was determined to be 816.54 $m^2 g^{-1}$, which is lower than that of HKUST-1 (855.52 $m^2 g^{-1}$). This may be due to the fact that part of the thioacetamide molecules entered the cavity of MOF, forming Cu-S species and reducing its pore cage, which eventually leads to a slight decrease in the BET surface area[13]. Above characterization results have clearly shown the existence of the isolated Cu-S motif in HKUST-1 precatalyst. We speculate that the S heteroatoms generated from the thioacetamide might locally replace the flanking water molecule (O_w) attached to the Cu atoms and break the Cu-O_w bonds without destroying the long-range order of HKUST-1[22b].

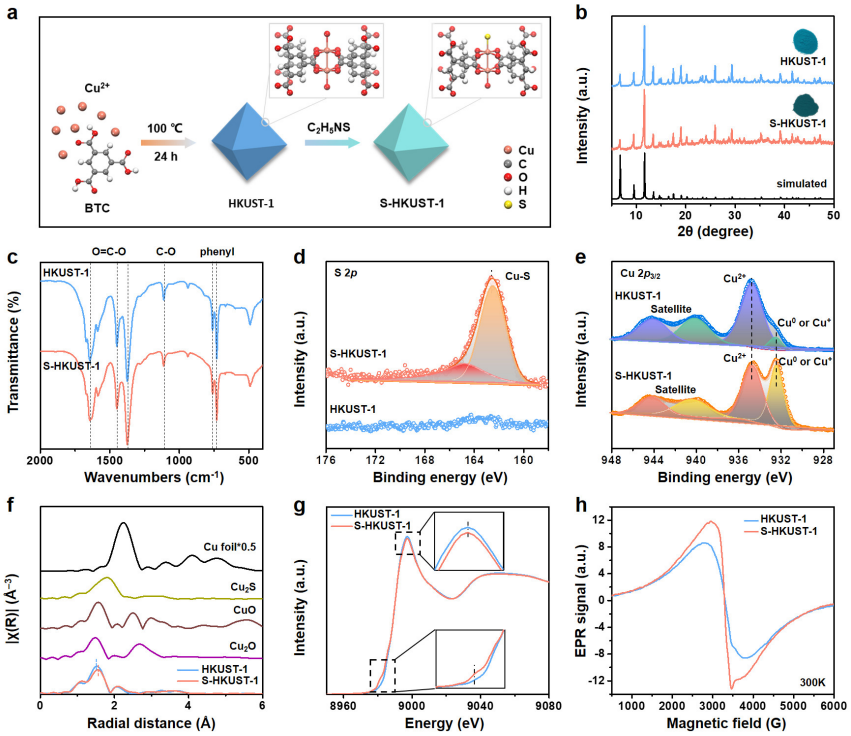

Figure 1. (a) Schematic illustration of the preparation of S-HKUST-1, which indicates the local H_2O molecule might be replaced by S heteroatoms. (b) XRD patterns of the prepared S-HKUST-1 and HKUST-1 precatalysts, which are well indexed to the simulated HKUST-1. The insets are digital photos of S-HKUST-1 (dark green) and HKUST-1 (blue). (c) FTIR spectra of S-HKUST-1 and HKUST-1 precatalysts, indicating negligible difference. The XRD and FTIR results prove that the long-range ordered structure has not been destroyed after S incorporation. (d, e) High-resolution XPS spectra of S-HKUST-1 and HKUST-1 precatalysts in (d) S_{2p} region, showing the characteristic Cu-S bonds in the S-HKUST-1 precatalyst and (e) Cu_{2p} region, showing the increased content of Cu^+ or Cu^0 species. (f) FT of the EXAFS spectra and (g) Cu K-edge XANES spectra of HKUST-1 and S-HKUST-1 precatalysts. The inset of (g) is the magnified image. The XAFS results in (f, g) prove the successful incorporation of local heteroatoms, which might be bonded to Cu atoms in MOFs. (h) EPR spectra of the samples measured at 300 K.

Electrocatalytic activity and selectivity evaluation of CO_2RR

The electrochemical CO_2RR performance was firstly evaluated using a gas-tight H-type cell, with S-HKUST-1 or HKUST-1 samples decorated glassy carbon electrode, Ag/AgCl and Pt mesh as working electrode, reference electrode and counter electrode, respectively (see more details in the Methods). We firstly studied the effects of different incorporated S contents, and their corresponding electrocatalytic CO_2RR selectivity results (biased at -1.22 to -1.52 V *vs*. RHE, potentials were referenced to RHE if not mentioned, and all potentials were not *iR*-corrected) illustrate that as the incorporated S contents increase, the FE_{C2H4} gradually increases; however, when the S content further increases, the FE_{C2H4} is significantly reduced (Figure S12). In addition, the excess S incorporated sample of CuS obtained from

vulcanization shows a poor selectivity towards CO_2RR (Figures S12c and S12d), which proves the critical role of isolated Cu-S motif in the S-HKUST-1 precatalyst. The CO_2RR activities of the optimized S-HKUST-1 and pristine HKUST-1 were summarized in Figure 2. Linear sweep voltammetry (LSV) curves for S-HKUST-1 and HKUST-1 were conducted in a CO_2-saturated 0.1 M $KHCO_3$ aqueous solution (Figure 2a). The S-HKUST-1 shows higher reduction current densities relative to HKUST-1. The liquid products were collected and analyzed by using ^1H nuclear magnetic resonance (NMR) spectroscopy. As shown in Figure S13, no obvious detectable liquid products were produced, which might be attributed to ultralow content of liquid products in the H-type cell. Figure S14 exhibits the distribution of CO_2RR gas products at different applied potentials on S-HKUST-1. For S-HKUST-1, the FE_{C2H4} maintains values of above 50.0% in a range of potentials from -1.22 to -1.42 V, and are higher than that of HKUST-1 (Figure 2b and Table S7). A maximum FE_{C2H4} of 60.0±2.0% can be reached at -1.32 V, while this value of HKUST-1 is only 24.4±2.1% (Figure 2b). The electrochemical active surface area (ECSA) for S-HKUST-1 and HKUST-1 were measured (Figure S15). To compare the intrinsic activity for CO_2RR, the ECSA-normalized *j* of C_2H_4 was obtained (Figure 2c). It reveals that the higher activity for ethylene production on S-HKUST-1 than HKUST-1. The Nyquist plots in Figure S16 reveal that S-HKUST-1 is characterized with a lower interfacial charge-transfer resistance (R_{ct}) than HKUST-1, evidencing a faster electron transfer from the electrodes to CO_2 during CO_2RR process[10b, 23], which may also contribute to the higher catalytic *j* of S-HKUST-1 than the HKUST-1 control (Figures 2a and 2c).

The reaction rate of CO_2RR might be limited by mass transport due to the low solubility of CO_2 in the H-type cell[24]. Thus, we further evaluated the CO_2RR performance of S-HKUST-1 in a flow cell system with 1.0 M KOH as electrolyte (Figure 2d, digital photos were shown in Figure S17). H_2, C_1 and C_2 products were formed on bare copper and HKUST-1 controls, and the FEs of H_2 and C_1 products decreased and C_2 products increased over S-HKUST-1 (Figure 2e and Tables S8-S10). The C_2 products include ethylene, ethanol, acetate, and among them, ethylene is the major product (Figure S18). For comparison, the FE_{C2H4} on bare Cu and HKUST-1 electrodes are generally below 40% over the current densities from 100 to 500 mA cm^{-2} (Figure S19 and Tables S8-S10). The FE_{C2H4} on S-HKUST-1 is obviously higher than that of HKUST-1 across the j range from 100 to 500 mA cm^{-2}. At the *j* of 400 mA cm^{-2}, H_2 selectivity remains below 20% FE, whereas the FE towards C_2H_4 surpasses 57.2% with the C_2H_4 partial *j* of 228 mA cm^{-2} (Figures 2e and S20). This is the highest selectivity of C_2H_4 and the highest C_2H_4 partial *j* among the Cu-based organometallic catalysts and MOFs; furthermore, the S-HKUST-1 also shows comparable C_2H_4 selectivity and activity among the reported Cu-based electrocatalysts (Table S11). When we used the S-HKUST-1 precatalyst, the Faradaic efficiency of overall C_2 product is 70.0~88.4% from 100 to 500 mA cm^{-2}, with peak selectivity of C_2 products towards FE of 88.4% at 400 mA cm^{-2}, which is higher than those of the bare Cu and HKUST-1 electrodes (Figure S21). Noteworthy, the S-HKUST-1 also demonstrates good electrocatalytic stability, retaining nearly unchanged FE of C_2H_4 (~50%) at an applied *j* of 150 mA cm^{-2} in a flow cell reactor (Figure 2f). Taken together, we demonstrate that isolating Cu-S motif in the HKUST-1 precatalyst could subtly activate the C_2H_4 performance.

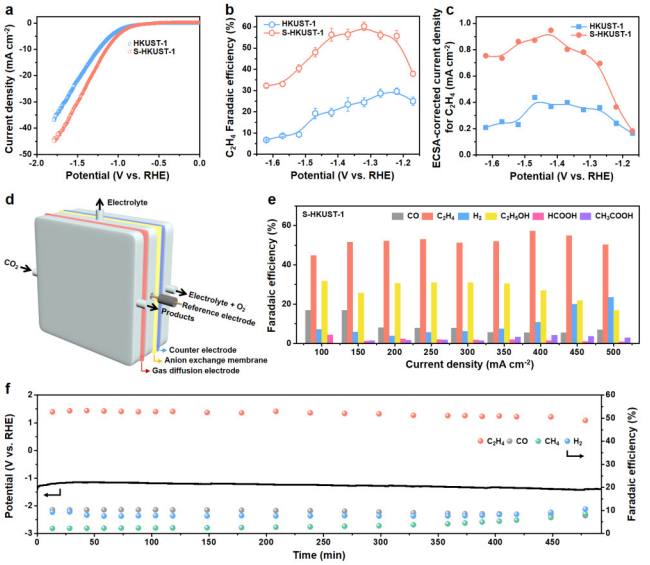

Figure 2. (a) LSV curves in the CO_2-saturated 0.1 M $KHCO_3$ aqueous solution at a scan rate of 10 mV s^{-1} for S-HKUST-1 and HKUST-1. The S-HKUST-1 shows larger catalytic current density relative to HKUST-1. (b) FE of C_2H_4 and (c) ECSA-normalized *j* of C_2H_4 for S-HKUST-1 and HKUST-1 in the CO_2-saturated 0.1 M $KHCO_3$ at various applied potentials. (d) Schematic illustration of the flow cell reactor. (e) FEs of products with S-HKUST-1 precatalysts at various applied *j* ranging from 100 to 500 mA cm^{-2} in liquid-electrolyte flow cell reactor. FE of CH_4 is below 1% at all applied *j* and was not plotted. (f) Long-time stability of S-HKUST-1 in 1.0 M KOH at an applied *j* of 150 mA cm^{-2} in a flow cell reactor, showing stable activity and selectivity for C_2H_4 over 480 min.

Structural evolution of the precatalyst

We firstly conducted *ex-situ* characterizations to study the structural evolution before and after CO_2RR (after reacting in CO_2-saturated 0.1 M $KHCO_3$ at a potential of -1.32 V for 1 h) over the precatalysts. In order to avoid the oxidation of copper as much as possible, the entire cell was transferred to the nitrogen glove box immediately after CO_2RR (Figure S22). The XPS spectra of the S-HKUST-1 precatalyst given in Figure S23a show that the peak of Cu^{2+} species centered at 934.7 eV was disappeared, which indicates that the valence states of Cu changed from Cu^{2+} to Cu^+/Cu^0 after CO_2RR[25]. Further surface state analysis was performed with a Cu LMM auger peak, which shows the Cu^+ auger peak at 570.0 eV and Cu^0 peaks at 567.9 eV (Figure S23b) [19]. It is obvious that both Cu^0 and Cu^+ states are present on the surface of the catalyst after the CO_2RR. In the XRD pattern, the S-HKUST-1 precatalyst has lost the characteristic diffraction peaks of original MOFs, but exhibits typical diffraction peaks of Cu(111) and Cu(200) at 43.3° and 50.4° (PDF 04-0836), which is consistent with the XPS results (Figure S24). Concomitantly, the morphological changes are revealed by the TEM images of S-HKUST-1 and HKUST-1 precatalysts after CO_2RR, which indicates that both samples have changed from the initial micron sized octahedral particles to the final dendritic morphologies (Figures 3a, S25a and S26a), which is consistent with the SEM results (Figures S27). Moreover, the high-resolution transmission electron microscopy (HRTEM) images (Figures 3b, S25 and S26) display the lattice fringes with a spacing distance of 2.08 Å, which is corresponding to the Cu(111) crystal planes, also demonstrating that the Cu ion in precatalysts have been reduced

to metallic Cu during CO_2RR process. The HAADF-STEM and corresponding EDS elemental maps show that Cu and S elements distributed homogeneously throughout the whole catalyst structure (Figures 3c and S26d-S26e). We further replaced the Nafion solution with an anion solution (Sustainion® XA9 Ionomer solution), which doesn't contain the sulfur element. The EDS analysis revealed that sulfur also exist in the catalyst after CO_2RR, indicating that S element is derived from the S-HKUST-1 catalyst (Figure S28). The XPS result of S-HKUST-1 after CO_2RR also indicates the existence of S element, which is consistent with the above-mentioned characterizations (Figure S29 and S30). We speculate that the regenerative Cu(S) matrix during CO_2RR might give abundant Cu/Cu_xS_y interfaces on the atomic level local structure.

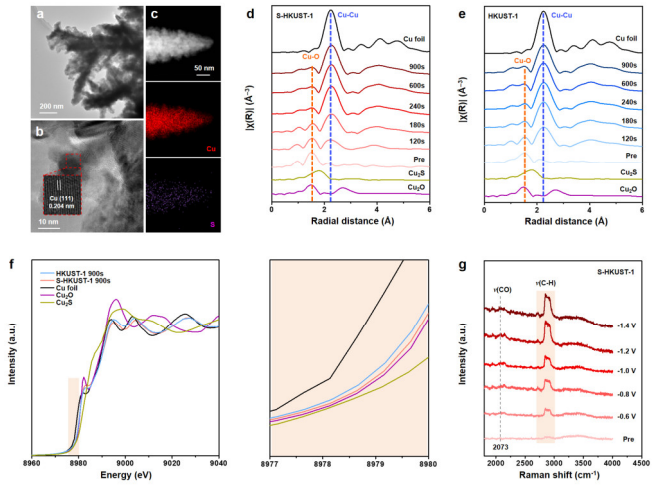

Figure 3. (a) TEM and (b) HRTEM images of S-HKUST-1 collected after CO_2RR electrocatalysis process. The inset of (b) is the enlarged HRTEM image showing the Cu(111) lattice fringe. (c) HAADF-STEM image for S-HKUST-1 after CO_2RR electrocatalysis and corresponding EDS elemental maps of Cu, S and mix. (d, e) Operando FT Cu K-edge EXAFS spectra with respect to time for (d) S-HKUST-1 and (e) HKUST-1 precatalysts under an applied potential of -1.30 V in CO_2-saturated 0.1 M $KHCO_3$. (f) Operando Cu K-edge XANES spectra of S-HKUST-1 and HKUST-1 after 15 minutes of reaction at -1.30 V vs. RHE in 0.1 M $KHCO_3$. (g) *In-situ* Raman spectra of S-HKUST-1 during CO_2RR at different potentials in CO_2-saturated 0.1 M $KHCO_3$.

In order to further study the local coordination environments and chemical states of the S-HKUST-1 and HKUST-1 under realistic CO_2RR conditions, operando X-ray absorption fine structure (XAFS) analysis was performed[26]. In the operando EXAFS spectra for S-HKUST-1 and HKUST-1 precatalysts, the intensity of the Cu-O peak gradually decreases and the intensity of the Cu-Cu peak gradually increases (Figures 3d and 3e). This result confirms that the formed Cu^0 species are regenerative from Cu^{2+} species in S-HKUST-1 and HKUST-1 precatalysts. In the operando XANES spectra in the Cu K-edge for S-HKUST-1 and HKUST-1 precatalysts at the working potential of -1.30 V (Figure S31), the curves of S-HKUST-1 and HKUST-1 gradually become similar to that of the Cu foil reference as the CO_2RR continues, suggesting that the pristine main components of Cu^{2+} in S-HKUST-1 and HKUST-1 are reduced to low-valent Cu during CO_2RR testing conditions, which is consistent with recently reported results for HKUST-1 precatalysts[16, 25b, 27]. In particular, the comparison of Cu K-edge adsorption of S-HKUST-1 and HKUST-1 catalysts with the reference samples suggests that the average oxidation states of Cu in S-HKUST-1 and HKUST-1 derived catalysts lie between 0 and +1 after 15 minutes of reaction at -1.30 V (Figure 3f). Furthermore, the absorption edge of S-HKUST-1 is on the higher energy side than that of HKUST-1, implying the higher Cu oxidation state[28]. The result show that the regenerative Cu(S) matrix derived from predesigned S-HKUST-1 features more oxidized $Cu^{\delta+}$ species than the HKUST-1 control, which might give abundant active sites for C_2 products generation.

In-situ Raman measurement was carried out to further investigate the origins of the excellent CO_2RR performance of S-HKUST-1. A custom-built Raman setup was used to probe the surface of S-HKUST-1 and HKUST-1 during CO_2RR at different potentials in CO_2-saturated 0.1 M $KHCO_3$ (Figure S32). The vibration of C-H on S-HKUST-1 and HKUST-1 was observed in the area at 2700-3000 cm^{-1} (Figures 3g and S33).[29] The peaks are more obvious on S-HKUST-1 than that on HKUST-1, indicating that more reaction intermediates containing C-H bonds are produced on S-HKUST-1. Remarkably, S-HKUST-1 catalyst significantly improved the formation of key hydrocarbon intermediates, which might promote the subsequent C-C coupling step and thus the production of hydrocarbons.

Theoretical studies of biphasic Cu/Cu_xS_y interface

To elucidate the superior selectivity of Cu(S) matrix on catalyzing CO_2RR into C_2 products, we further performed the density functional theory (DFT) calculations to reveal the inherent mechanism (see the calculation details in the Methods). Essentially, it has been widely regarded that the bound *CO intermediate (* denotes an adsorption site) is the key species in the formation of both C_1 and C_2 products[30], and the *CO hydrogenation (*CO + *H → *COH/*CHO + *) versus the dimerization process (2*CO → *OCCO + *) serving as the rate-limiting steps (RLS) largely limits the selectivity of C_2 formation[31], which is confirmed by the thermodynamic energy profiles for these two processes computed over the Cu(111) surface (Figure 4a; see more details in Figure S34 and Table S12). Thus, we focused on these two elementary steps for comparison to understand the CO_2RR activity and selectivity on Cu(S) matrix. Regarding the construction of Cu(S) matrix, the possible structures are diverse including stoichiometric and non-stoichiometric sulfide phases. However, because of the experimental characterization on the valence states of surface and bulk Cu (around 0 ~ 1), the stoichiometric Cu(S) systems are ruled out (*i.e.*, CuS and Cu_2S). Estimated from the thermodynamic phase diagrams in Figure S35, the binary Cu/Cu_2S interface structure can be expected to dominantly exist, and thus we constructed the Cu/Cu_2S interface for modelling the realistic active site eventually (Figure S36, see more details in the Methods). Notably, the average charge of Cu atoms near the optimized Cu/Cu_2S interface is 0.14 |e| from the Bader charge analysis, indicating that these Cu sites are in the form of partially oxidized $Cu^{\delta+}$, which is in line with the experimental observation.

The *CO dimerization step was calculated at the Cu/Cu_2S interface (Figure 4c). The effect of realistic solution environment is considered in the calculation, in which explicit water layers are introduced over the catalyst to simulate the liquid/solid interface by invoking the ab initio molecular dynamics (AIMD) simulations

(Figure S37). Figure 4d illustrates the located transition state, in which the *OC…CO* intermediate is stabilized by the neighboring H_2O molecules via hydrogen bonds, and the corresponding barrier is calculated to be 0.67 eV. In comparison, this barrier is lower than that over Cu(111) (0.91 eV, close to the calculation of Sargent et al. [30a]), suggesting that the activity of oxidized $Cu^{\delta+}$ at the Cu/Cu_2S interface is higher than pure metal Cu(111) for C_2 production. Moreover, the bulk Cu_2S with high concentration of S atoms was examined and found less active for *CO dimerization because of the long distance between Cu-Cu cations (3.927 Å), which prevented the *CO intermediates from bonding together, and this is also consistent with the experimental result. Therefore, we conclude that the Cu/Cu_2S interface with isolated Cu-S motif is active for catalyzing CO_2RR into C_2 product. The energy barrier for *CO hydrogenation to C_1 products at the Cu/Cu_2S interface was also calculated to be 1.04 eV for generating *CHO intermediates (Figures 4c and 4d). Compared with *OCCO formation, this barrier is higher by 0.37 eV, demonstrating the more favorable C_2 production than C_1 at Cu/Cu_2S interface.

To understand the intrinsic nature of Cu(S) matrix for good C_2 selectivity in depth, the geometric and electronic structures were further analyzed. As shown in Figure 4e, the distance between Cu^0 and $Cu^{\delta+}$ sites at Cu/Cu_2S interface is modest, even a little smaller than that on pure Cu(111) surface (2.458 Å vs. 2.579 Å), which conduces to the easy *CO dimerization geometrically. Moreover, as illustrated in Figure S38, *CO occupies the hollow-site and interacts with three Cu atoms (i.e., two Cu^0 and one $Cu^{\delta+}$) at the Cu/Cu_2S interface, in which the interface $Cu^{\delta+}$ takes a Bader charge 0.14 |e|. Based on the crystal orbital Hamilton populations (-COHP) and integrated -COHP (-ICOHP) analysis (Figure 4b), the -ICOHP of $Cu^{\delta+}$-CO bond at the Cu/Cu_2S interface rises continuously and reaches a relatively steady value (~1.55 eV) at the Fermi level, which is smaller than that of Cu^0-CO bond (1.61 eV) on Cu(111) surface. The smaller -ICOHP value demonstrates a weaker interaction between *CO species and $Cu^{\delta+}$ in comparison with the metallic Cu^0 site. Quantitatively, the adsorption energy at the Cu/Cu_2S interface is -1.12 eV (-0.51 eV considering temperature effect at 298 K), which is weaker by 0.29 eV than that on Cu(111) surface. In other word, the presence of partially oxidized $Cu^{\delta+}$ at the Cu/Cu_2S interface weakens the *CO adsorption and thus facilitates the CO dimerization to C_2 products.

In addition, regarding previous studies reported S-modified copper catalyst for formate product, we also did some first-principles calculations to verify the peculiarity of our catalyst structure on reaction products. The CO_2 adsorption via the carbon atom instead of di-oxygen generally serves as a key precursor for *COOH formation[32], and it tends to be further hydrogenated into *CO intermediate rather than the formate product. For our catalyst, it mainly comprises of a majority of metallic Cu^0 with abundant Cu/Cu_2S interfaces, which might be different from the S-modified catalysts reported in previous studies[33]. At the interface Cu region, the computational result shows that CO_2 tends to adsorb into $*CO_2^-$ species via carbon atom rather than the di-oxygen atoms. Specifically, we calculated the progress of *COOH formation from $*CO_2^-$ species, and the reaction barrier is only 0.10 eV with an enthalpy change of -0.66 eV (Figure S39). These *COOH intermediates can be further hydrogenated into *CO, a widely accepted precursor prior to creating C_2 products[34]. On the contrary, S-modified copper will weaken the CO_2 adsorption and suppress the formation of *CO intermediate. Also, previous studies suggested that the sulfur doping on the copper surface could suppress the HER owing to the slower combined desorption rate of H_2[33]; accordingly, the formate production competes with HER for surface accumulated H*, possibly via a Heyrovsky-like mechanism into $HCOO^-$ product[35].

In light of these analysis above, the superior selectivity of S-HKUST-1 precatalyst on catalyzing CO_2RR into C_2 product, compared with copper or copper sulfide, can be rationalized: benefited from the approximate Cu^0-$Cu^{\delta+}$ distance, *CO dimerization step can easily occur at the Cu/Cu_2S interface, and excessively high S-content catalysts (*i.e.*, Cu_2S) features with the long Cu-Cu distance, geometrically hindering the *CO dimerization; the Cu/Cu_2S interface presents a weakened binding energy to *CO species, which prompts the *CO dimerization than pure metallic Cu catalyst.

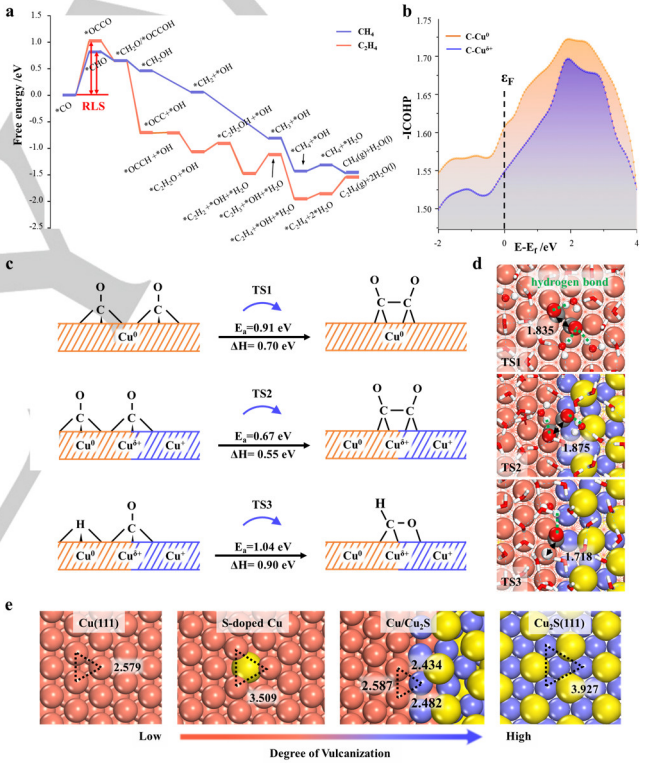

Figure 4. (a) Calculated free energy profiles for CO_2RR to CH_4 and C_2H_4 over pure Cu(111) surface, indicating the initial *CO hydrogenation and dimerization steps basically determine the CH_4 and C_2H_4 products distribution. Detailed geometries and energetic information are listed in Figure S35 and Table S12. (b) Integrated crystal orbital Hamilton populations (-ICOHPs) curves for $Cu^{\delta+}$-CO and Cu^0-CO bonds. (c) The reaction barriers together with enthalpies, and (d) corresponding transition states configuration for *CO dimerization and hydrogenation over Cu(111) and Cu/Cu_2S surfaces, respectively. Yellow, red, gray, white, orange and blue balls refer to S, O, C, H, Cu^0 and $Cu^{\delta+}$ atoms, respectively. (e) Surface configuration (top view) of Cu-based structures with different degrees of vulcanization. The distances between two neighboring Cu atoms on different surfaces are labeled, respectively (in Å).

Conclusion

In this work, we develop a rational predesign strategy to isolate stable Cu-S motif into the HKUST-1 precatalyst. The regenerative Cu(S) matrix exhibits a high C_2H_4 selectivity up to 57.2% at the operated a *j* of 400 mA cm^{-2}. This is the best selectivity and activity value for C_2H_4 among the Cu-based metalorganic and MOFs for CO_2RR electrocatalysts. The operando XAFS analysis along with systematic characterizations demonstrate the stable Cu-S motif during CO_2RR, which can be stabilize more active $Cu^{\delta+}$ species. The theoretical results further illustrate the significant importance of the S stabilized $Cu^{\delta+}$ at the Cu/Cu_xS_y interface with optimized geometric and electronic structures for $^*CO$ dimerization. We believe this work opens up a new avenue to finely predesign precatalysts with stable and active species for C_2 products-selective electrocatalysts.

Acknowledgements

This work was financially supported by the International (Regional) Cooperation and Exchange Projects of the National Natural Science Foundation of China (51920105003), the National Natural Science Funds for Distinguished Young Scholars (51725201), the Innovation Program of Shanghai Municipal Education Commission (E00014), the National Natural Science Foundation of China (51902105, 21873028, 22072045), the Shanghai Engineering Research Center of Hierarchical Nanomaterials (18DZ2252400) and the Shanghai Sailing Program (19YF1411600). The authors acknowledge the support by Shanghai Rising-star and Shuguang Programs (20QA1402400, 17SG30). The authors acknowledge the Fundamental Research Funds for the Central Universities (JKD01211519, JKVJ1211022). Additional support was provided by the Feringa Nobel Prize Scientist Joint Research Center. The authors also thank the Frontiers Science Center for Materiobiology and Dynamic Chemistry. The authors also thank the crew of the BL14W1 beamline at the Shanghai Synchrotron Radiation Facility (SSRF) and the 1W1B beamline of Beijing Synchrotron Radiation Facility (BSRF) for their constructive assistance with the XAFS measurements and data analyses.

Keywords: CO_2 electrocatalysis; ethylene-selective; isolated Cu-S motif; operando XAFS; precatalyst

[1] a) M. Aresta, A. Dibenedetto, A. Angelini, *Chem. Rev.* **2014**, *114*, 1709-1742; b) C. Chen, J. F. Khosrowabadi Kotyk, S. W. Sheehan, *Chem* **2018**, *4*, 2571-2586; c) Z. W. Seh, J. Kibsgaard, C. F. Dickens, I. Chorkendorff, J. K. Nørskov, T. F. Jaramillo, *Science* **2017**, *355*, eaad4998.

[2] a) H. Mistry, A. S. Varela, S. Kühl, P. Strasser, B. R. Cuenya, *Nat. Rev. Mater.* **2016**, *1*, 16009; b) O. S. Bushuyev, P. De Luna, C. T. Dinh, L. Tao, G. Saur, J. van de Lagemaat, S. O. Kelley, E. H. Sargent, *Joule* **2018**, *2*, 825-832; c) W. Zhou, K. Cheng, J. Kang, C. Zhou, V. Subramanian, Q. Zhang, Y. Wang, *Chem. Soc. Rev.* **2019**, *48*, 3193-3228; d) A. Vasileff, C. Xu, Y. Jiao, Y. Zheng, S.-Z. Qiao, *Chem* **2018**, *4*, 1809-1831.

[3] M. G. Kibria, J. P. Edwards, C. M. Gabardo, C. T. Dinh, A. Seifitokaldani, D. Sinton, E. H. Sargent, *Adv. Mater.* **2019**, *132*, 18130-18139.

[4] a) D. Gao, R. M. Arán-Ais, H. S. Jeon, B. Roldan Cuenya, *Nat. Catal.* **2019**, *2*, 198-210; b) H. Li, T. Liu, P. Wei, L. Lin, D. Gao, G. Wang, X. Bao, *Angew. Chem. Int. Ed.* **2021**, *60*, 14329-14333; *Angew. Chem.* **2021**, *133*, 14450-14454; c) Z. Z. Niu, F. Y. Gao, X. L. Zhang, P. P. Yang, R. Liu, L. P. Chi, Z. Z. Wu, S. Qin, X. Yu, M. R. Gao, *J. Am. Chem. Soc.* **2021**, *143*, 8011-8021.

[5] H. Mistry, A. S. Varela, C. S. Bonifacio, I. Zegkinoglou, I. Sinev, Y. W. Choi, K. Kisslinger, E. A. Stach, J. C. Yang, P. Strasser, B. R. Cuenya, *Nat. Commun.* **2016**, *7*, 12123.

[6] W. Zhang, C. Huang, Q. Xiao, L. Yu, L. Shuai, P. An, J. Zhang, M. Qiu, Z. Ren, Y. Yu, *J. Am. Chem. Soc.* **2020**, *142*, 11417-11427.

[7] T.-T. Zhuang, Z.-Q. Liang, A. Seifitokaldani, Y. Li, P. De Luna, T. Burdyny, F. Che, F. Meng, Y. Min, R. Quintero-Bermudez, C. T. Dinh, Y. Pang, M. Zhong, B. Zhang, J. Li, P.-N. Chen, X.-L. Zheng, H. Liang, W.-N. Ge, B.-J. Ye, D. Sinton, S.-H. Yu, E. H. Sargent, *Nat. Catal.* **2018**, *1*, 421-428.

[8] C. W. Li, M. W. Kanan, *J. Am. Chem. Soc.* **2012**, *134*, 7231-7234.

[9] a) F. S. Roberts, K. P. Kuhl, A. Nilsson, *Angew. Chem. Int. Ed.* **2015**, *54*, 5179-5182; b) D. Gao, I. Zegkinoglou, N. J. Divins, F. Scholten, I. Sinev, P. Grosse, B. Roldan Cuenya, *ACS Nano* **2017**, *11*, 4825-4831.

[10] a) Z.-Q. Liang, T. T. Zhuang, A. Seifitokaldani, J. Li, C. W. Huang, C. S. Tan, Y. Li, P. De Luna, C. T. Dinh, Y. Hu, Q. Xiao, P. L. Hsieh, Y. Wang, F. Li, R. Quintero-Bermudez, Y. Zhou, P. Chen, Y. Pang, S. C. Lo, L. J. Chen, H. Tan, Z. Xu, S. Zhao, D. Sinton, E. H. Sargent, *Nat. Commun.* **2018**, *9*, 3828; b) Y. Zhou, F. Che, M. Liu, C. Zou, Z. Liang, P. De Luna, H. Yuan, J. Li, Z. Wang, H. Xie, H. Li, P. Chen, E. Bladt, R. Quintero-Bermudez, T. K. Sham, S. Bals, J. Hofkens, D. Sinton, G. Chen, E. H. Sargent, *Nat. Chem.* **2018**, *10*, 974-980; c) T. Qin, Y. Qian, F. Zhang, B.-L. Lin, *Chinese Chem. Lett.* **2019**, *30*, 314-318.

[11] a) S. Dang, Q.-L. Zhu, Q. Xu, *Nat. Rev. Mater.* **2018**, *3*, 17075; b) L. Yang, X. Zeng, W. Wang, D. Cao, *Adv. Funct. Mater.* **2018**, *28*, 1704537; c) W. Xia, A. Mahmood, R. Zou, Q. Xu, *Energy & Environ. Sci.* **2015**, *8*, 1837-1866; d) C. Yan, H. Li, Y. Ye, H. Wu, F. Cai, R. Si, J. Xiao, S. Miao, S. Xie, F. Yang, Y. Li, G. Wang, X. Bao, *Energy & Environ. Sci.* **2018**, *11*, 1204-1210; e) Z. Jiang, X. Xu, Y. Ma, H. S. Cho, D. Ding, C. Wang, J. Wu, P. Oleynikov, M. Jia, J. Cheng, Y. Zhou, O. Terasaki, T. Peng, L. Zan, H. Deng, *Nature* **2020**, *586*, 549-554.

[12] a) T. Shinagawa, G. O. Larrazábal, A. J. Martín, F. Krumeich, J. Pérez-Ramírez, *ACS Catal.* **2018**, *8*, 837-844; b) K. R. Phillips, Y. Katayama, J. Hwang, Y. Shao-Horn, *J. Phys. Chem. Lett.* **2018**, *9*, 4407-4412.

[13] K. Cho, S.-H. Han, M. P. Suh, *Angew. Chem. Int. Ed.* **2016**, *55*, 15301-15305; *Angew. Chem.* **2016**, *128, 1*5527-15531.

[14] Y. C. Tan, H. C. Zeng, *Nat. Commun.* **2018**, *9*, 4326.

[15] S. S.-Y. Chui, S. M.-F. Lo, J. P. H. Charmant, A. G. Orpen, I. D. Williams, *Science* **1999**, *283*, 1148-1150.

[16] D.-H. Nam, O. S. Bushuyev, J. Li, P. De Luna, A. Seifitokaldani, C.-T. Dinh, F. P. Garcia de Arquer, Y. Wang, Z. Liang, A. H. Proppe, C. S. Tan, P. Todorovic, O. Shekhah, C. M. Gabardo, J. W. Jo, J. Choi, M. J. Choi, S.-W. Baek, J. Kim, D. Sinton, S. O. Kelley, M. Eddaoudi, E. H. Sargent, *J. Am. Chem. Soc.* **2018**, *140*, 11378-11386.

[17] D. Wakerley, S. Lamaison, F. Ozanam, N. Menguy, D. Mercier, P. Marcus, M. Fontecave, V. Mougel, *Nat. Mater.* **2019**, *18*, 1222-1227.

[18] a) C. Zhao, G. Luo, X. Liu, W. Zhang, Z. Li, Q. Xu, Q. Zhang, H. Wang, D. Li, F. Zhou, Y. Qu, X. Han, Z. Zhu, G. Wu, J. Wang, J. Zhu, T. Yao, Y. Li, H. J. M. Bouwmeester, Y. Wu, *Adv. Mater.* **2020**, *32*, 2002382; b) C. G. Morales-Guio, E. R. Cave, S. A. Nitopi, J. T. Feaster, L. Wang, K. P. Kuhl, A. Jackson, N. C. Johnson, D. N. Abram, T. Hatsukade, C. Hahn, T. F. Jaramillo, *Nat. Catal.* **2018**, *1*, 764-771; c) N. Martić, C. Reller, C. Macauley, M. Löffler, B. Schmid, D. Reinisch, E. Volkova, A. Maltenberger, A. Rucki, K. J. J. Mayrhofer, G. Schmid, *Adv. Energy Mater.* **2019**, *9*, 1901228; d) J. Kim, W. Choi, J. W. Park, C. Kim, M. Kim, H. Song, *J. Am. Chem. Soc.* **2019**, *141*, 6986-6994.

[19] S. Y. Lee, H. Jung, N. K. Kim, H. S. Oh, B. K. Min, Y. J. Hwang, *J. Am. Chem. Soc.* **2018**, *140*, 8681-8689.

[20] K. Yao, Y. Xia, J. Li, N. Wang, J. Han, C. Gao, M. Han, G. Shen, Y. Liu, A. Seifitokaldani, X. Sun, H. Liang, *J. Mater. Chem. A* **2020**, *8*, 11117-11123.

[21] C. Prestipino, L. Regli, J. G. Vitillo, F. Bonino, A. Damin, C. Lamberti, A. Zecchina, P. L. Solari, K. O. Kongshaug, S. Bordiga, *Chem. Mater.* **2006**, *18*, 1337-1346.

[22] a) C. Huang, J. Dong, W. Sun, Z. Xue, J. Ma, L. Zheng, C. Liu, X. Li, K. Zhou, X. Qiao, Q. Song, W. Ma, L. Zhang, Z. Lin, T. Wang, *Nat. Commun.* **2019**, *10*, 2779; b) A. E. Baumann, G. E. Aversa, A. Roy, M. L. Falk, N. M. Bedford, V. S. Thoi, *J. Mater. Chem. A* **2018**, *6*, 4811-4821.

[23] a) X. Li, W. Bi, M. Chen, Y. Sun, H. Ju, W. Yan, J. Zhu, X. Wu, W. Chu, C. Wu, Y. Xie, *J. Am. Chem. Soc.* **2017**, *139*, 14889-14892; b) C. F. Wen, F. Mao, Y. Liu, X. Y. Zhang, H. Q. Fu, L. R. Zheng, P. F. Liu, H. G. Yang, *ACS Catal.* **2020**, *10*, 1086-1093.

[24] a) L.-C. Weng, A. T. Bell, A. Z. Weber, *Energy & Environ. Sci.* **2019**, *12*, 1950-1968; b) J. Gu, C.-S. Hsu, L. Bai, H. M. Chen, X. Hu, *Science* **2019**, *364*, 1091-1094.

[25] a) Q. Zhu, D. Yang, H. Liu, X. Sun, C. Chen, J. Bi, J. Liu, H. Wu, B. Han, *Angew. Chem. Int. Ed.* **2020**, *59*, 8896-8901; b) Q. Zhu, X. Sun, D. Yang, J. Ma, X. Kang, L. Zheng, J. Zhang, Z. Wu, B. Han, *Nat. Commun.* **2019**, *10*, 3851.

[26] a) S.-C. Lin, C.-C. Chang, S.-Y. Chiu, H.-T. Pai, T.-Y. Liao, C.-S. Hsu, W.-H. Chiang, M.-K. Tsai, H. M. Chen, *Nat. Commun.* **2020**, *11*, 3525; b) T. Möller, F. Scholten, T. N. Thanh, I. Sinev, J. Timoshenko, X. Wang, Z. Jovanov, M. Gliech, B. Roldan Cuenya, A. S. Varela, P. Strasser, *Angew. Chem. Int. Ed.* **2020**, *59*, 17947-17983; *Angew. Chem.* **2020**, *132*, 18130-18139; c) B. Mei, S. Gu, X. Du, Z. Li, H. Cao, F. Song, Y. Huang, Z. Jiang, *X-Ray Spectrom.* **2020**, *49*, 251-259.

[27] Z. Weng, Y. Wu, M. Wang, J. Jiang, K. Yang, S. Huo, X. F. Wang, Q. Ma, G. W. Brudvig, V. S. Batista, Y. Liang, Z. Feng, H. Wang, *Nat. Commun.* **2018**, *9*, 415.

[28] W. Ma, S. Xie, T. Liu, Q. Fan, J. Ye, F. Sun, Z. Jiang, Q. Zhang, J. Cheng, Y. Wang, *Nat. Catal.* **2020**, *3*, 478-487.

[29] a) J. Gao, H. Zhang, X. Guo, J. Luo, S. M. Zakeeruddin, D. Ren, M. Gratzel, *J. Am. Chem. Soc.* **2019**, *141*, 18704-18714; b) Y. Song, J. R. C. Junqueira, N. Sikdar, D. Ohl, S. Dieckhofer, T. Quast, S. Seisel, J. Masa, C. Andronescu, W. Schuhmann, *Angew. Chem. Int. Ed.* **2021**, *60*, 9135-9141; *Angew. Chem.* **2021**, *133*, 9217-9224.

[30] a) P. De Luna, R. Quintero-Bermudez, C.-T. Dinh, M. B. Ross, O. S. Bushuyev, P. Todorović, T. Regier, S. O. Kelley, P. Yang, E. H. Sargent, *Nat. Catal.* **2018**, *1*, 103-110; b) K. J. P. Schouten, Y. Kwon, C. J. M. van der Ham, Z. Qin, M. T. M. Koper, *Chem. Sci.* **2011**, *2*, 1902-1909; c) X. Nie, M. R. Esopi, M. J. Janik, A. Asthagiri, *Angew. Chem. Int. Ed.* **2013**, *52*, 2459-2462.

[31] a) J. H. Montoya, C. Shi, K. Chan, J. K. Nørskov, *J. Phys. Chem. Lett.* **2015**, *6*, 2032-2037; b) K. Jiang, R. B. Sandberg, A. J. Akey, X. Liu, D. C. Bell, J. K. Nørskov, K. Chan, H. Wang, *Nat. Catal.* **2018**, *1*, 111-119; c) J. Hussain, H. Jónsson, E. Skúlason, *ACS Catal.* **2018**, *8*, 5240-5249.

[32] J. Wang, H. Y. Tan, Y. Zhu, H. Chu, H. M. Chen, *Angew. Chem. Int. Ed.* **2021**, *60*, 17254-17267; *Angew. Chem.* **2021**, *133*, 17394-17407.

[33] Y. Huang, Y. Deng, A. D. Handoko, G. K. L. Goh, B. SiangYeo, *ChemSusChem* **2018**, *11*, 320-326.

[34] H. Xiao, W. A. Goddard, 3rd, T. Cheng, Y. Liu, *Proc. Natl. Acad. Sci. U. S. A.* **2017**, *114*, 6685-6688.

[35] R. Garcia-Muelas, F. Dattila, T. Shinagawa, A. J. Martin, J. Perez-Ramirez, N. Lopez, *J. Phys. Chem. Lett.* **2018**, *9*, 7153-7159.

Entry for the Table of Contents

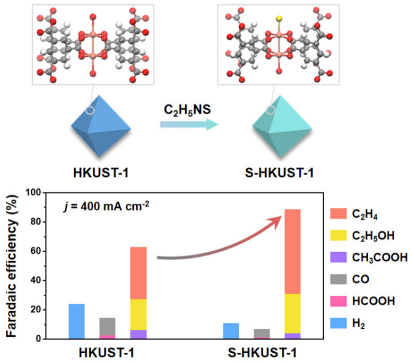

The S-HKUST-1 precatalyst with a stable isolated Cu-S motif was prepared by local sulfur doping strategy, which can be *in-situ* reconstructed to obtain Cu(S) matrix with active biphasic copper/copper sulfide interfaces, delivering a current density of 400 mA cm^{-2} with Faradaic efficiency of ethylene to 57.2% in the flow cell.